Concurrent promotion of phase transition and bimetallic nanocatalyst exsolution in perovskite oxides driven by Pd doping to achieve highly active bifunctional fuel electrodes for reversible solid oxide electrochemical cells

Kyeong Joon Kim [a],[1], Chaesung Lim [b],[1], Kyung Taek Bae [a],[1], Jong Jun Lee [c], Mi Young Oh [d], Hyung Jun Kim [b], Hyunmin Kim [e], Guntae Kim [e], Tae Ho Shin [d],[*], Jeong Woo Han [b],[*], Kang Taek Lee [a],[f],[*]

[a] Department of Mechanical Engineering, KAIST, Daejeon 34141, Republic of Korea
[b] Department of Chemical Engineering, POSTECH, Pohang, Gyeongbuk 37673, Republic of Korea
[c] Department of Energy Science and Engineering, DGIST, Daegu 42988, Republic of Korea
[d] Korea Institute of Ceramic Engineering and Technology, KICET, 101 Soho-Ro, 52851, Jinju, Republic of Korea
[e] Department of Energy and Chemical Engineering, UNIST, Ulsan 44919, Republic of Korea
[f] KAIST Institute for the NanoCentury, KAIST, Daejeon 34141, Republic of Korea

ARTICLE INFO

ABSTRACT

The reducibility of B-site elements in perovskite (ABO$_3$) structures is one of the paramount factors that promote the *in-situ* exsolution of metallic nanocatalysts, and the phase transition of the support to a more stable structure under solid oxide cell (SOC) fuel electrode operating conditions. Herein, we develop a highly catalytically active and durable perovskite-based fuel electrode material—La$_{0.6}$Sr$_{0.4}$Co$_{0.15}$Fe$_{0.8}$Pd$_{0.05}$O$_{3-\delta}$ (LSCFP)—for reversible SOCs. The LSCFP material under the fuel electrode condition is fully transformed into a stable Ruddlesden-Popper phase decorated by bimetallic Co-Fe nanocatalysts. The SOC with LSCFP fuel electrode yielded outstanding performances in both fuel cell (2.00 W cm^{-2}) and electrolysis cell (2.23 A/cm^2 at 1.3 V) modes at 850 °C, with remarkable reversible-cyclic stability. These results clearly demonstrate that the novel LSCFP capable of concurrent phase transition and bimetallic exsolution in the reducing condition is a highly prospective candidate as a bifunctional fuel electrode for reversible SOCs.

1. Introduction

Solid oxide cells (SOCs) are highly efficient electrochemical energy conversion devices which can operate reversibly in fuel cell (FC) mode to generate electricity and in electrolysis cell (EC) mode to convert electrical energy from renewable sources into useful fuels [1].

State-of-the-art SOCs rely on Ni-based fuel electrodes because of their excellent electrical conductivity and high catalytic activity for both water splitting and hydrogen dissociation reactions under typical operating conditions [2]. However, Ni-based fuel electrodes suffer from severe performance degradation during long-term operation caused by Ni coarsening [3]. Furthermore, during abrupt changes to the redox

conditions—which occur during emergency shutdown, interruption of fuel supply, and inhomogeneous distribution of fuel flow in practical SOC stacks—Ni-based electrodes experience volume changes and cracking at the electrode/electrolyte interface, leading to the failure of the SOC.

Therefore, as alternative fuel electrode materials, perovskite-based oxide catalysts have been researched thoroughly because of the high redox stability and compositional flexibility that can be attained by doping elements in the A and B sites to tune the catalytic activity [4]. Moreover, one straightforward strategy to further improve the performance of perovskite-based electrodes is surface modification with nanoparticle catalysts [5]. Conventionally, these nano-sized catalysts

---

have been decorated on the backbone material *via* an infiltration technique, in which a suspension containing target metal precursors is coated on the surface of the mother oxide. However, this process usually requires multiple complex deposition steps. Moreover, the control of the final morphology and distribution of these nanoparticles on the surface of the random and porous electrodes is limited and still challenging [6].

Recently, a more cost-effective, single-step, and efficient 'exsolution' process by which the nano-scale metallic catalysts are spontaneously formed directly from the perovskite oxide lattice in reducing conditions has been proposed. Compared to the conventional infiltration method, the exsolved nanoparticles are strongly anchored and exhibit inherently improved distribution with superior size uniformity on the perovskite oxide support, resulting in greatly enhanced catalytic activity and durability [7]. In addition, the reversible exsolution and dissolution of metal nanoparticles in backbones under redox conditions has been demonstrated as a key characteristic for providing superior retention of high catalytic activity against nanoparticle aggregation and coke formation [8].

Exsolution in perovskite families is usually reported in two cases: (1) A-site-deficient perovskites ($A_{1-\alpha}BO_3$) and (2) stoichiometric perovskites (ABO_3). For instance, Irvine et al. repeatedly demonstrated that decreasing the stoichiometry of various perovskite-based materials (from $A/B = 1$ to $A/B < 1$) effectively promotes highly concentrated exsolution of B-site metal nanoparticles by lowering the activation energy of the phase separation and precipitation [9]. In the case of stoichiometric perovskite materials, highly reducible B-site transition metals can be destabilized into lower valence states under a reducing atmosphere, resulting in the spontaneous exsolution of the B-site elements on the lattice surface along with reconstruction of the bulk crystal structure into other perovskite-related structures (*e.g.*, A_2BO_4, $A_2B_2O_5$) [10,11]. Chung et al. reported that, under reducing conditions, a Mn-doped $La_{0.6}Sr_{0.4}FeO_3$ perovskite anode exhibited *in-situ* phase transformation to a Ruddlesden-Popper (RP) phase ($La_{1.2}Sr_{0.8}Mn_{0.4}Fe_{0.6}O_4$) with metallic Fe nanoparticle exsolution, resulting in ~ 10 times higher maximum power density (MPD, 0.72 W cm^{-2}) compared to conventional $La_{0.8}Sr_{1.2}FeO_4$ at 800 °C in H_2 (0.07 W cm^{-2}) [7]. More recently, Kim et al. demonstrated that the $La_{0.6}Sr_{0.4}Co_{0.2}Fe_{0.8}O_3$ (LSCF) perovskite, which is one of the most widely used oxygen electrodes for SOCs, was transformed into RP-phase $La_{1.2}Sr_{0.8}Co_{0.12}Fe_{0.88}O_4$ with exsolved Co-Fe alloy nanoparticles under the fuel electrode condition, and the SOC with the LSCF fuel electrode exhibited quite acceptable FC performance of 0.73 W cm^{-2} in MPD at 800 °C [12].

While mechanistic understanding of the exsolution accompanying phase transformation in stoichiometric perovskites is limited, previous research implies that reducibility of the B-site elements is one of the key factors that trigger the exsolution of B-site transition metals, as well as phase transition into stable structures under SOC fuel electrode operating conditions [13]. Thus, we expect that if highly reducible elements,

such as Pd, are properly doped at the B-site of the perovskite lattice, this dopant can act as a 'promoter' to subsequently lower the activation energy of the reduction of the other B-site transition metals, concurrently enhancing the exsolution of the B-site cations along with the phase transition under reducing conditions. In this regard, this Pd-doped perovskite can facilitate both hydrogen oxidation (HOR) and evolution reactions (HER) as a fuel electrode for reversible SOCs, as shown in Fig. 1.

To demonstrate this concept, we prepared a novel fuel electrode by Pd-doping into the perovskite LSCF ($La_{0.6}Sr_{0.4}Co_{0.15}Fe_{0.8}Pd_{0.05}O_{3-\delta}$, LSCFP). The crystallographic phase evolution, oxidation state change of constituent elements, and reducing behavior of LSCFP under SOC operating conditions were systematically investigated. For further fundamental understanding, we attempted to study the role of Pd doping in LSCF on exsolution and phase transition in a reducing atmosphere *via* density functional theory (DFT) calculations at the atomic scale. Finally, SOCs employing the LSCFP fuel electrode was fabricated and their electrochemical performances were gauged in both FC and EC modes, demonstrating the feasibility of LSCFP as a promising fuel electrode for reversible SOCs.

2. Experimental

2.1. Materials synthesis

LSCF and LSCFP were prepared *via* sol-gel process. An appropriate stoichiometric ratio of $La(NO_3)_3.6 H_2O$ (99.9%, Alfa Aesar), $Sr(NO_3)_2$ (99.99%, Sigma Aldrich), $Co(NO_3)_2.6 H_2O$ (99.99%, Alfa Aesar), and $Fe(NO_3)_3.9 H_2O$ (99.99%, Alfa Aesar) were dissolved in de-ionized water by stirring for 2 h. LSCFP was produced by the same method, with the addition of $Pd(OCOCH_3)_2$ (99.999%, Sigma Aldrich) that had been dissolved in acetone media until transparent. Subsequently, each reactant suspension was mixed and evaporated at 130 °C to form a gel. The gels were dried at 400 °C for 1 h to remove the organic components. Each sample was pulverized using mortar and pestle, and calcined at 1200 °C for 5 h to get a black powder.

2.2. Cell fabrication

For the fabrication of the electrode pastes, both LSCF and LSCFP powders were mixed with an ink system (ESL 441, ESL Electro Science) at a ratio of 50:50 wt%. For symmetric cells, dense $La_{0.8}Sr_{0.2}Ga_{0.8}Mg_{0.2}O_{3-\delta}$ (LSGM, Kceracell, Korea) pellets were fabricated by uniaxial pressing, followed by sintering at 1450 °C for 10 h. The LSCF or LSCFP pastes were coated on both sides of the dense LSGM substrate and sintered at 1050 °C for 3 h. For the SOC test, an LSCF-GDC (Rhodia, USA) composite (50:50 wt%) was used as the oxygen electrode on the $\sim$ 300-μm-thick LSGM electrolyte support. The fuel electrode (*i.e.*, LSCF or
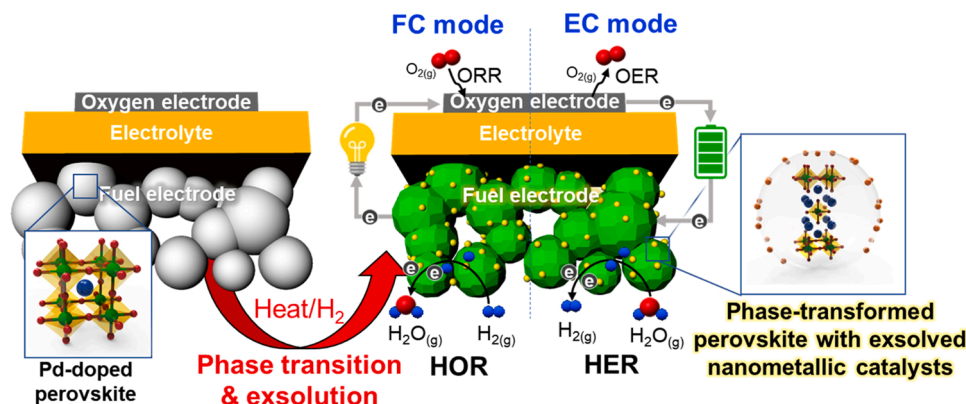

Fig. 1. Schematic diagram of the proposed Pd-doped perovskite as a fuel electrode for a solid oxide cell.

LSCFP) and LSCF-GDC oxygen electrode were painted on both sides of the LSGM pellet. The electrodes were continuously fired at 1050 °C for 3 h. The active area of oxygen electrode for the SOC was ~ 0.5 cm^2. An Ag mesh (52 mesh, Alpha Aesar, USA) that was connected to each electrode using Ag-Pd ink (ESL Electro Science, USA) acted as a current collector.

2.3. Characterization

Powder XRD measurement was performed using an X-ray diffractometer (RIGAKU, SmartLab) over a 2θ range of 20–80° with Cu Kα radiation (λ = 1.5418 Å). The crystal structure of each powder was refined and determined using the HighScore software. The refinement parameters were unit cell parameters, background, and scale factors. *In-situ* XRD was performed under a H$_2$ atmosphere at temperatures of 100–850 °C with increments of 50 °C, holding the samples at the reaction temperature for 2 h. The H$_2$ temperature programmed reduction (TPR) was conducted using a BELCAT-M instrument (BEL, Japan Inc.). The LSCF and LSCFP samples were heated with He gas at 1000 °C for 1 h before H$_2$-TPR analysis. The flow rate and heating rate were 10% H$_2$/Ar at 40 ml min^{-1} and 10 °C min^{-1}, respectively.

The microstructures of the electrode surfaces and cross-sections were observed using field emission scanning electron microscopy (SEM, S-4800, Hitachi). The high-resolution morphology of the materials was determined by transmission electron microscopy (TEM, HF-3300, Hitachi) equipped with an energy dispersive X-ray spectroscopy (EDS) system (Bruker Co., model QUANTAX-200). X-ray photoelectron spectroscopy (XPS, ESCALAB 250, VG SCIENTIFIC) analysis was conducted to investigate the valance states of the elements in the LSCF and LSCFP powders.

The electrode resistance of the fabricated symmetric cells (~ 2-mm-thick LSGM electrolyte with ~ 30-μm-thick LSCF and LSCFP electrodes) was evaluated in the temperature range of 650–850 °C using a potentiostat (VMP-300, Bio-Logic). Moreover, redox cycling tests were performed on the LSCFP electrode at 750 °C.

To investigate the current-voltage (I-V) characteristics of the LSCFP fuel electrode, the SOCs were loaded into the in-house single-cell measurement system and kept airtight. Subsequently, the electrochemical performance of the SOCs was evaluated using a potentiostat. For the FC and EC performance, humidified H$_2$ gas was fed at concentrations of 3% and 50% H$_2$O (200 sccm), respectively, by controlling the temperature of the water bubbler into the fuel electrode. Moreover, dry air (200 sccm) was supplied into the oxygen electrode for both measurements.

2.4. Computational details

All the theoretical studies were performed by spin-polarized DFT with the Vienna *ab initio* simulation package (VASP) and projector-augmented wave pseudopotentials [14,15]. The generalized gradient approximation (GGA) proposed by Perdew, Burke, and Ernzerhof (PBE) was used as the exchange-correlation energy functional [16]. The cutoff energy for the plane wave was set to be 400 eV. Electronic occupancies were calculated by the Gaussian smearing with a smearing parameter of 0.05 eV. The GGA+U approach was used to correct the self-interaction errors with U_{eff} = 4.0 and 3.3 eV for the Fe 3d and Co 3d orbitals, respectively [11,17]. All the calculations were performed until the forces on each atom were within 0.03 eV/Å based on a force-based conjugate gradient algorithm. For the Brillouin zones of the bulk model of cubic perovskite (1 × 1 × 2 supercell), rhombohedral perovskite (2 × 2 × 1 supercell), and the RP phase (1 × 1 × 1 unit cell), 3 × 3 × 1, 2 × 2 × 1, and 3 × 3 × 1 Monkhorst−Pack k-point sampling were used, respectively. For the Brillouin zones of the slab model of cubic perovskite (1 × 1 surface unit cell, 8 layers, vacuum layer of 15 Å), rhombohedral perovskite (1 × 1 surface unit cell, 4 layers, vacuum layer of 15 Å), and the RP phase (1 × 1 surface unit cell, 12 layers, vacuum layer of 17 Å), 3 × 3 × 1, 1 × 1 × 1, and 2 × 2 × 1 Monkhorst−Pack

k-point sampling were used, respectively [18]. For the bulk layer in the slab model, the three bottom layers were fixed. The optimized lattice constants of the LSCF and LSCFP are summarized in Table S1. The total energy differences between the simple perovskite and RP phases were calculated using the following equation:

$$E_{Total\ energy\ difference} = \frac{1}{16}E_{RP} + \frac{1}{2}E_{B-metal} + \frac{1}{2}E_{O_2} - \frac{1}{16}E_{simple\ perov} \quad (1)$$

where E_{RP} and $E_{simple\ perov}$ are the total energies of the RP phase (1 × 1 × 1 unit cell) and simple perovskite (1 × 1 × 2 supercell), respectively, $E_{B-metal}$ is the total energy of B-metal crystals (BCC Fe, HCP Co, and FCC Pd), and E_{O_2} is the total energy of the gas-phase oxygen molecule.

The oxygen vacancy formation energies were calculated by the following equation

$$E_{vf} = E_{perov-defect} + \frac{1}{2}E_{O_2} - E_{perov} \quad (2)$$

where $E_{perov-defect}$ and E_{perov} are the total energies of perovskite with and without the oxygen vacancy, respectively.

To study the exsolution mechanism of the Co-Fe alloy, segregation energy ($E_{segregation}$), co-segregation energy ($E_{co-segregation}$),[11] and alloy formation energy ($E_{alloy-formation}$) were calculated using the following equations:

$$E_{segregation(x-O-y)} = E_{x-O-y_{surface}} - E_{x-O-y_{bulk}} \quad (3)$$

$$E_{co-segregation(x-O_{vac}-y)} = E_{x-O_{vac}-y_{surface}} - E_{x-O_{vac}-y_{bulk}} \quad (4)$$

$$E_{alloy-formation} = \frac{1}{2}(2 \times E_{Co-O_{vac}-Fe} - E_{Co-O_{vac}-Co} - E_{Fe-O_{vac}-Fe}) \quad (5)$$

where $E_{A-O-B_{surface}}$ and $E_{A-O-B_{bulk}}$ are the total energy of the structures in which the A-oxygen-B pair is located at the surface and in the bulk respectively. $E_{A-O_{vac}-B_{surface}}$ and $E_{A-O_{vac}-B_{bulk}}$ are the total energy of the structures where the A-oxygen vacancy-B pair is located at the surface and in the bulk, respectively.

3. Results and discussion

3.1. Crystallographic phase analysis

Fig. 2a-d show the refined X-ray diffraction (XRD) patterns of the LSCFP and LSCF powders before and after reduction in dry H$_2$ at 700 °C. The lattice parameters calculated from the refinement results are tabulated in Table 1. The goodness of fit ($χ^2$), defined as the average deviation in refinement with the calculated model, was used to confirm the agreement between the observed and calculated data. The $χ^2$ values for the pristine LSCF, reduced LSCF, pristine LSCFP, and reduced LSCFP powders were 0.7726, 1.2970, 0.9313, and 1.0930, respectively, indicating that the refinement results were convincing. Both the pristine LSCF (Fig. 2a) and LSCFP (Fig. 2b) powders had the same rhombohedral perovskite with a space group of R-3c. However, with 5 mol% Pd doping at the B-site, the lattice volume increased from 350.5768 Å^3 (pristine LSCF) to 351.6740 Å^3 (pristine LSCFP), which is reasonably explained by the larger ionic radius of Pd (0.86 Å) compared to that of Co^{2+}/Co^{3+} (0.61/0.65 Å) in 6-coordination. The doping amount of Pd for LSCFP was determined based on the XRD analysis with different amounts of Pd as shown in Fig. S1. In Fig. S2, the HR-TEM images of LSCF and LSCFP before reduction are shown. The interplanar distances of (110) for LSCF and LSCFP correspond to are 2.71 Å and 2.72 Å respectively, which are consistent with the theoretical d-spacing of (110) of the perovskite structure. Moreover, Fig. S3 shows the EDX spectra of LSCFP before reduction. Homogenous distribution of all constituent elements (La, Sr, Co, Fe, Pd, and O) revealed that the solid solution is properly formed without segregation nor phase decomposition. After reduction in H$_2$ at 700 °C, LSCF was composed of rhombohedral crystal structure
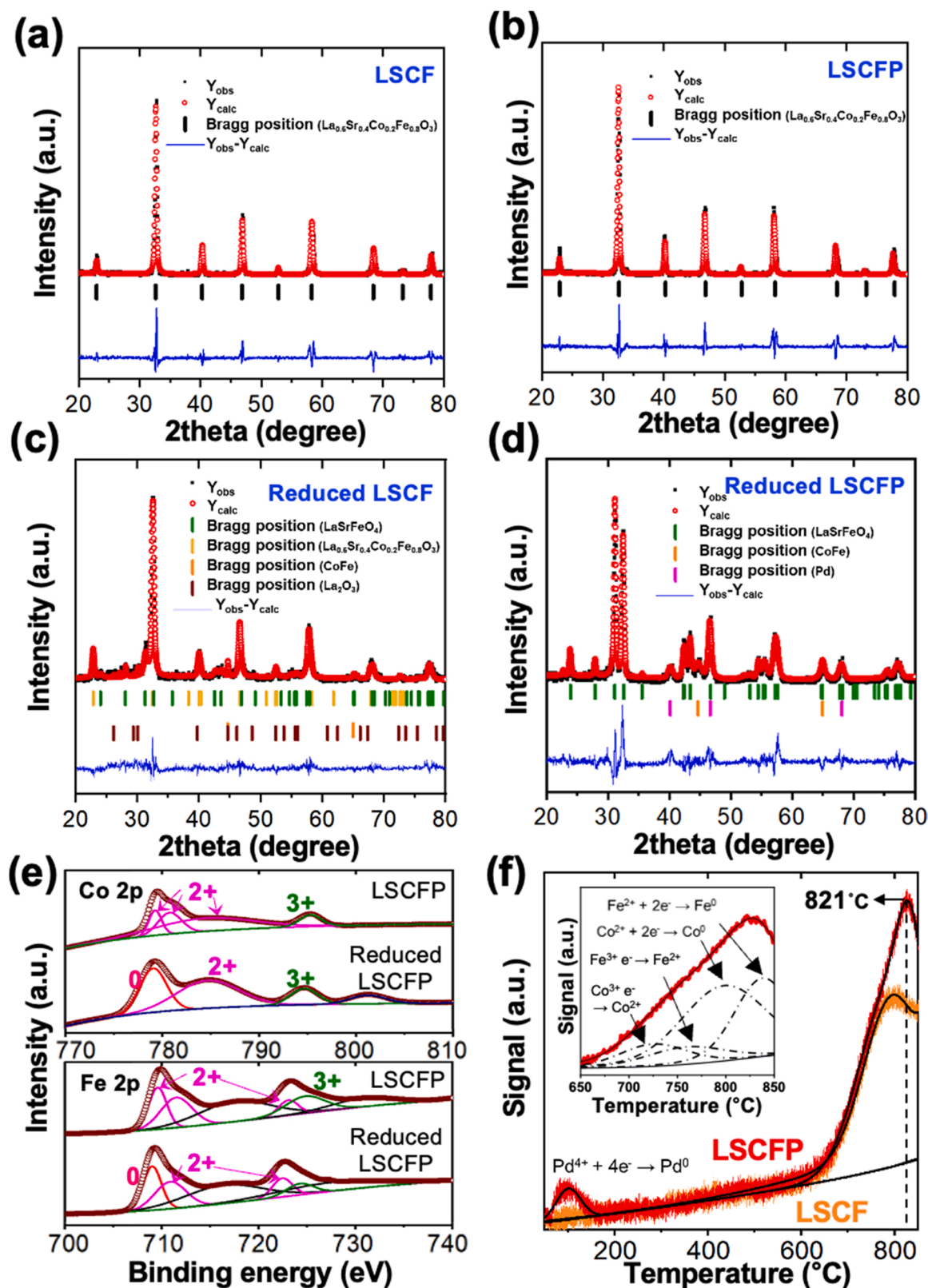
Fig. 2. Observed and calculated PXRD profiles: as-prepared (a) LSCF and (b) LSCFP, and reduced (c) LSCF and (d) LSCFP. (e) XPS spectra before and after the reduction of LSCFP and LSCF: Co 2p, and Fe 2p. (f) H_2-TPR results for LSCFP.

$(La_{0.6}Sr_{0.4}Co_{0.2}Fe_{0.8}O_3$ (R-3c)), trigonal crystal structure (La_2O_3 (Pm-3m1)), and the RP-type tetragonal phase ($LaSrFeO_4$, I4/mmm), in addition to small amounts of the Co-Fe alloy (Pm-3 m) phase (Fig. 2c), while at 800 °C it was transformed RP phase with minor peaks of Co-Fe

alloy and La_2O_3, which is consistent with other recent reports [12,19] (Fig. S4). On the other hand, in H_2 condition at 700 °C, LSCFP was fully transformed into the single RP phase of the tetragonal crystal structure ($LaSrFeO_4$, I4/mmm) with minor metallic phases of the Co-Fe alloy

Table 1
Lattice parameters derived from Rietveld refinement of the reduced LSCFP and LSCF at 700 °C.

Material	Condition	Phase	Crystal system	Space group	a [Å]	b [Å]	c [Å]	V [Å³]	R_{wp}	R_p	χ^2
LSCF	Pristine	$La_{0.6}Sr_{0.4}Co_{0.2}Fe_{0.8}O_3$	Rhombohedral	*R-3c* (167)	5.5002	5.502	13.3814	350.5768	0.2619	0.1760	0.7726
	Reduced	$LaSrFeO_4$	Tetragonal	*I4/mmm* (139)	3.8811	3.8811	12.7343	191.8160	0.1998	0.1423	1.2970
		$La_{0.6}Sr_{0.4}Co_{0.2}Fe_{0.8}O_3$	Rhombohedral	*R-3c* (167)	5.5280	5.5280	13.4533	356.0373			
		Co-Fe	Cubic	*Pm-3m* (221)	2.8808	2.8808	2.8808	23.9078			
		La_2O_3	Trigonal	*P-3m1* (164)	3.9296	3.9296	6.1667	82.4970			
LSCFP	Pristine	$La_{0.6}Sr_{0.4}Co_{0.2}Fe_{0.8}O_3$	Rhombohedral	*R-3c* (167)	5.5080	5.5080	13.3856	351.6940	0.1883	0.1314	0.9313
	Reduced	$LaSrFeO_4$	Tetragonal	*I4/mmm* (139)	3.8880	3.8880	12.7396	192.5787	0.1989	0.1395	1.0930
		Co-Fe	Cubic	*Pm-3m* (221)	2.8536	2.8536	2.8536	23.2370			
		Pd	Cubic	*Fm-3m* (225)	3.8642	3.8642	3.8642	57.7004			

(Pm-3 m) and Pd (Fm-3 m) (Fig. 2d). These results indicate that 5 mol% Pd doping into the B-site of LSCF perovskite highly promoted phase transition from the perovskite to the RP phase under the reducing condition at lower temperature.

3.2. Oxidation states of elements

Fig. 2e and S5a-b show the valence states of Co, Fe, and Pd in the LSCF and LSCFP powders, respectively, identified by XPS measurement. To analyze the reduction behaviors of the two materials, both samples were heat treated in a 100% H_2 atmosphere at 700 °C for 2 h. Prior to deconvolution of the XPS peak of each sample, we subtracted the C 1 s peak of the carbon set as the reference and baseline. Subsequently, the elemental spectra of the samples were programmed using the Origin software. The calculated relative number of oxidation states for each element are summarized in Table 2. The upper parts of Fig. 2e and S5a compare the Co 2p spectra of both samples. The characteristic peaks were located at binding energies of 792 and 780 eV, corresponding to Co $2p_{1/2}$ and Co $2p_{3/2}$, respectively [20]. In addition, one satellite peak was observed at 787.7 eV [21].

The binding energies of 779.9, 780.4 and 784.2 eV were corresponded to Co^{2+}, while the binding energies of 779.2 and 795.5 eV were assigned to Co^0 and Co^{3+}, respectively [22]. The Co 2p spectra of the pristine LSCFP and LSCF powders were dominated by Co^{2+}. After reduction, for both samples, some of the Co^{3+} cations were reduced to Co^{2+}, as evident from the area growth of the Co^{2+} peaks at the expense of the Co^{3+} peak areas. Furthermore, an additional peak was observed at 779.9 eV corresponding to Co^0, which indicates the presence of metallic Co [23]. For the Fe 2p spectra of the samples, the two main peaks at 724.6 and 709.3 eV were assigned to Fe $2p_{1/2}$ and Fe $2p_{3/2}$, respectively (lower part of Figs. 2e and S5a) [24]. These peaks were deconvoluted into six subpeaks. Among these, one peak at 724.9 eV was assigned to Fe^{3+}, three peaks (709.4, 711.4, and 723.1 eV) to Fe^{2+}, and another peak at 708.9 eV corresponded to Fe^0 [25]. The peaks with binding energies of 717.1 and 730.5 eV were satellite peaks of Fe 2p. Similar to Co, the Fe^{3+} cations were partially reduced to a lower valence state in H_2. After reduction, the average valence states of B-site transition metal elements (Co and Fe) decreased, while LSCFP exhibited a greater drop in oxidation states (*e.g.*, from +2.11 to +1.42 for Co) compared to LSCF (*e. g.*, from +2.24 to +1.95 for Co) as shown in Table 2. Fig. S5b shows the high-resolution spectrum of Pd 3d for the LSCFP samples. The peaks at

Pd 3d were located at binding energies of 336.7 and 342.2 eV, assigned to Pd $3d_{5/2}$ and Pd $3d_{3/2}$, respectively. For pristine LSCFP, Pd^{2+} (336.6 and 342.2 eV) and Pd^{4+} (337.7 eV) accounted for 82% and 18% of the total Pd content, respectively [26]. After reduction, Pd^{4+} and Pd^{2+} ions changed to Pd^0 (334.6, 335.4, 340.0, and 340.7 eV) [27].

Fig. S5c shows the O 1 s core levels XPS spectra of the samples. The O 1 s signal was deconvoluted into three components at 528.2, 530.5 and 532.5 eV, corresponding to lattice oxygen (O_L), adsorbed oxygen (O_A), and moisture oxygen (O_{H2O}), respectively [28]. The calculated ratios of O_A/O_L in the reduced LSCFP and LSCF samples were 0.862 and 0.805, respectively, indicating a high concentration of O_A species on the reduced LSCFP surface. It is known that these weakly bound O_A ions are readily released under reducing conditions at SOC operation temperatures, leading to the creation of oxygen vacancies and electrochemically active sites,[29] which is advantageous for the surface reaction of the fuel electrode. Before reduction, the averaged oxidation state of Pd corresponds to + 2.36, which is higher than those of Fe (+2.35) and Co (+2.24) in LSCF without Pd. As we believe, to compensate the higher oxidation state of Pd in LSFCP, the oxidation states of Fe and Co would decrease to + 2.25 and + 2.11, respectively, and also the concentration of oxygen vacancies, which are positively charged, were reduced in the as-calcined specimen. These results suggest that Pd doping in the perovskite LSCF effectively promoted the reducibility of B-site transition metal and exsolution of the Co-Fe alloy more effectively under a H_2 atmosphere.

3.3. Temperature dependent reduction behaviors

The H_2-TPR technique was used to investigate the reduction behavior of LSCFP from 50° to 850°C, as shown in Fig. 2f. Prior to analysis, the resultant data were fitted to solid lines. There were two H_2 consumption peaks centered at 100 and 821 °C. The low-temperature process at 100 °C was attributed to the reduction of Pd species from LSCFP, which has been consistently reported in previous studies [30]. Moreover, above 600 °C, the intense peak in two samples centered at 821°C was assigned to an overlapping reduction process combining $Co^{3+} + e^- \rightarrow Co^{2+}$, $Fe^{3+} + e^- \rightarrow Fe^{2+}$, $Co^{2+} + 2e^- \rightarrow Co^0$ and $Fe^{3+} + 2e^- \rightarrow Fe^0$, respectively [31,32]. Consumption peaks are often accompanied by a reduction in the high oxidation state as reported in previous studies [33]. The H_2-TPR results were in good agreement with the XRD (Fig. 1) and XPS (Fig. 2) analyses, indicating that LSCFP exsolved Co-Fe alloys

Table 2
Survey of LSCFP and LSCF valence states before and after reduction.

Material	Fe^0 (%)	Fe^{2+} (%)	Fe^{3+} (%)	Avg. valence state	Co^0 (%)	Co^{2+} (%)	Co^{3+} (%)	Avg. valence state	Pd^0 (%)	Pd^{2+} (%)	Pd^{4+} (%)	Avg. valence state	O_L (%)	O_A (%)
LSCFP	–	74.8	25.2	+2.25	–	89.4	10.6	+2.11	–	82.0	18.0	+2.36	50.3	49.7
LSCF	–	65.1	34.9	+2.35	–	76.3	23.7	+2.24	–	–	–	–	45.9	54.1
Reduced LSCFP	23.8	62.7	13.5	+1.66	35.5	51.3	13.2	+1.42	100	–	–	0	53.7	46.3
Reduced LSCF	11.2	62.6	17.2	+1.77	16.5	72.3	11.23	+1.78	–	–	–	–	52.1	45.7

more intensively than LSCF, with a small amount of metallic Pd under reducing conditions.

3.4. Nanoscale morphology analysis

Fig. 3a presents a bright-field TEM image of the reduced LSCFP powders at 700 °C, showing that a large number of ultrafine particles were exsolved on the parent particle surface. Higher magnification TEM
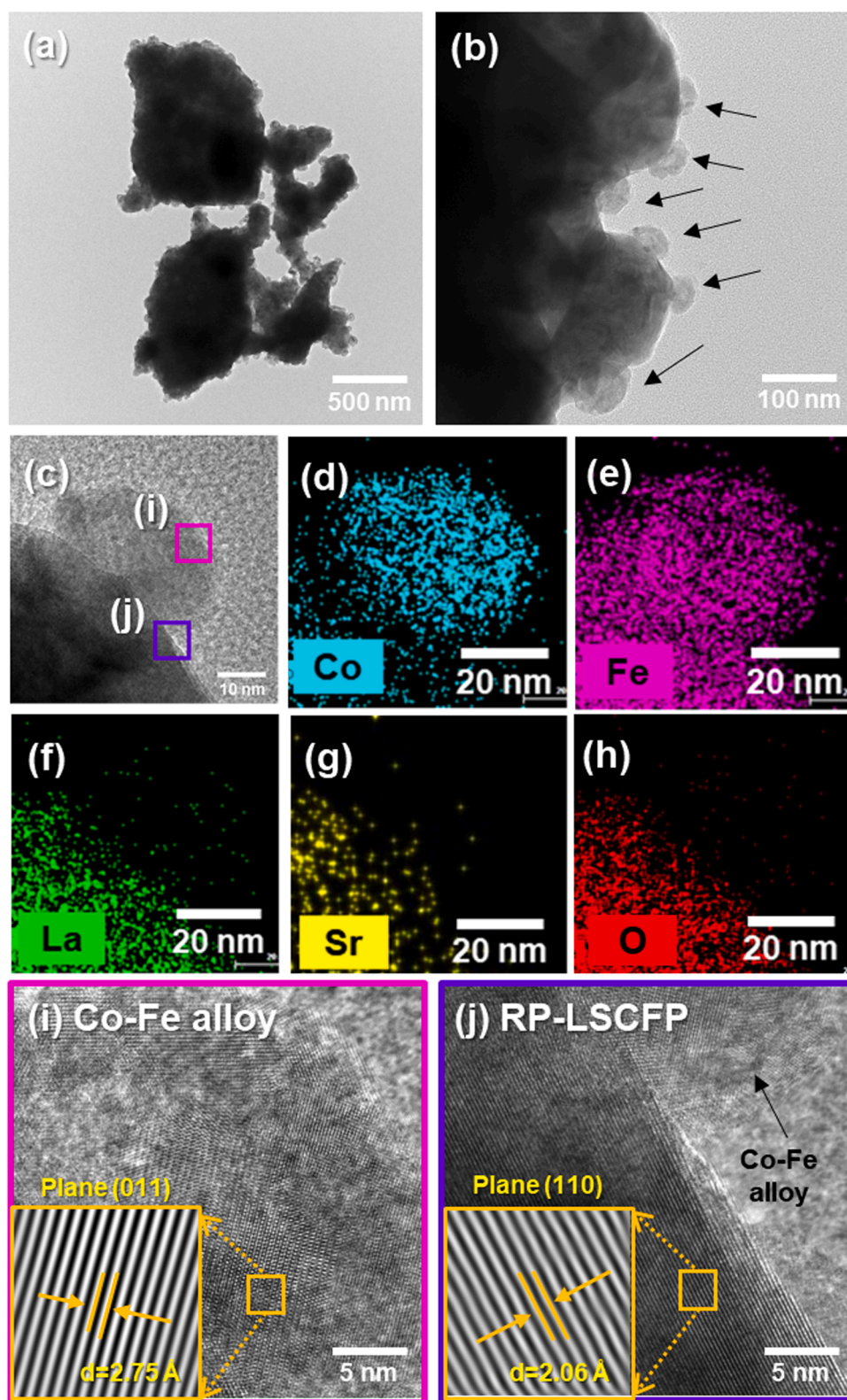

Fig. 3. (a, b) Bright-field, and (c) high-resolution TEM images of the reduced LSCFP powders. Elemental distribution of (d) Co, (e) Fe, (f) La, (f) Sr, and (h) O in (c). Magnified high-resolution TEM images of (i) Co-Fe nanoparticles and (j) RP-LSCFP matrix. Insets are the lattice fringe patterns.

images (Fig. 3b-c) clearly show that nano-sized particles with an average diameter of ~ 40 nm were periodically distributed on the LSCFP surface with firm adhesion at the interface. The elemental mapping images of the reduced LSCFP particles using TEM-EDS analysis are shown in Fig. 3d-h. Co, Fe, Sr, La, and O were uniformly distributed on the LSCFP support. In contrast, for the exsolved nanoparticles, only Co and Fe co-existed, indicating the formation of metallic Co-Fe alloy, consistent with the H$_2$-TPR results (Fig. 2f). To further investigate the crystallographic information, magnified HR-TEM images of the nanoparticle core (Fig. 3i) and exsolved particle/supporter interface regions (Fig. 3j) were acquired from the pink and purple square regions of Fig. 3c, respectively. The interplanar distance of each area was calculated using fast Fourier transformation (FFT). Then masking and filtering steps were performed with the Gatan Digital Micrograph software.

The inset of Fig. 3i shows that the interplanar spacing of the exsolved nanoparticles is 0.275 nm, corresponding to the (011) crystal planes of the Co-Fe alloy (space group Pm-3 m (221)). On the other hand, the interplanar distance of 0.206 nm of the LSCFP main particle region is consistent with the (110) planes of the RP structure (space group I4/mmm (139)) (Fig. 3j). These results confirmed the XRD analysis of the reduced LSCFP phase, as shown in Fig. 2d. In addition, we observed that metallic Pd nanoparticles were locally exsolved on the LSCFP surface (Fig. S6), but the number of Pd nanoparticles was much lower than that of Co-Fe alloy nanoparticles, primarily due to compositional differences between elements.

3.5. Theoretical interpretation

Density functional theory calculations were performed to reveal the role of the Pd dopant in phase transition and exsolution. The exsolution of Co-Fe alloy is closely related to the phase transition because they both experience a similar extraction process of Co, Fe, and oxygen in the lattice. When the phase transition energies of LSCF and LSCFP perovskites to RP-LSCF were compared, LSCFP required lower energy for the phase transition than LSCF (Fig. 4a–c), which indicates that the phase transition of LSCFP is thermodynamically easier than that of LSCF.

The role of the Pd dopant was also investigated by comparing the oxygen vacancy formation energies (E_{vf}) of LSCF and LSCFP (Fig. 4d). E_{vf} was calculated for the oxygen sites of Fe-O-Fe, Co-O-Fe, and Pd-O-Fe, which are all possible configurations in the BO$_2$ layer (Figs. S7, S8). E_{vf} was lower for the oxygen sites of Fe-O-Fe than for Co-O-Fe or Pd-O-Fe in both LSCF and LSCFP (Fig. 4d). When Pd was doped into the LSCF perovskite, E_{vf} dramatically decreased from positive to negative values for both Fe-O-Fe and Co-O-Fe (Fig. 4d). For these types of materials, the phase stability decreases as E_{vf} decreases because oxygen can be easily removed [34]. Therefore, the addition of Pd makes the LSCF perovskite unstable, thereby promoting the phase transition under reduction conditions. The decreases in E_{Diff} and E_{vf} of LSCFP are correlated with the phase transition with Pd doping.

The exsolution of the Co-Fe alloy occurred on the LSCFP perovskite during the phase transition. To elucidate the effects of Pd doping and phase transition on the exsolution, we compared the seven key energetics required for the exsolution of Co-Fe alloy on three surface models (LSCF, LSCFP, RP-LSCFP) (Table S2, Fig. 5a); I: bulk oxygen vacancy formation energy (E_{vf_bulk}), II: surface oxygen vacancy formation energy ($E_{vf\_surface}$), III: segregation energy of Co-O-Co, Fe-O-Fe ($E_{segregation}$), IV: co-segregation energy of Co-O$_V$-Co, Fe-O$_V$-Fe ($E_{co-segregation}$), V: alloy co-
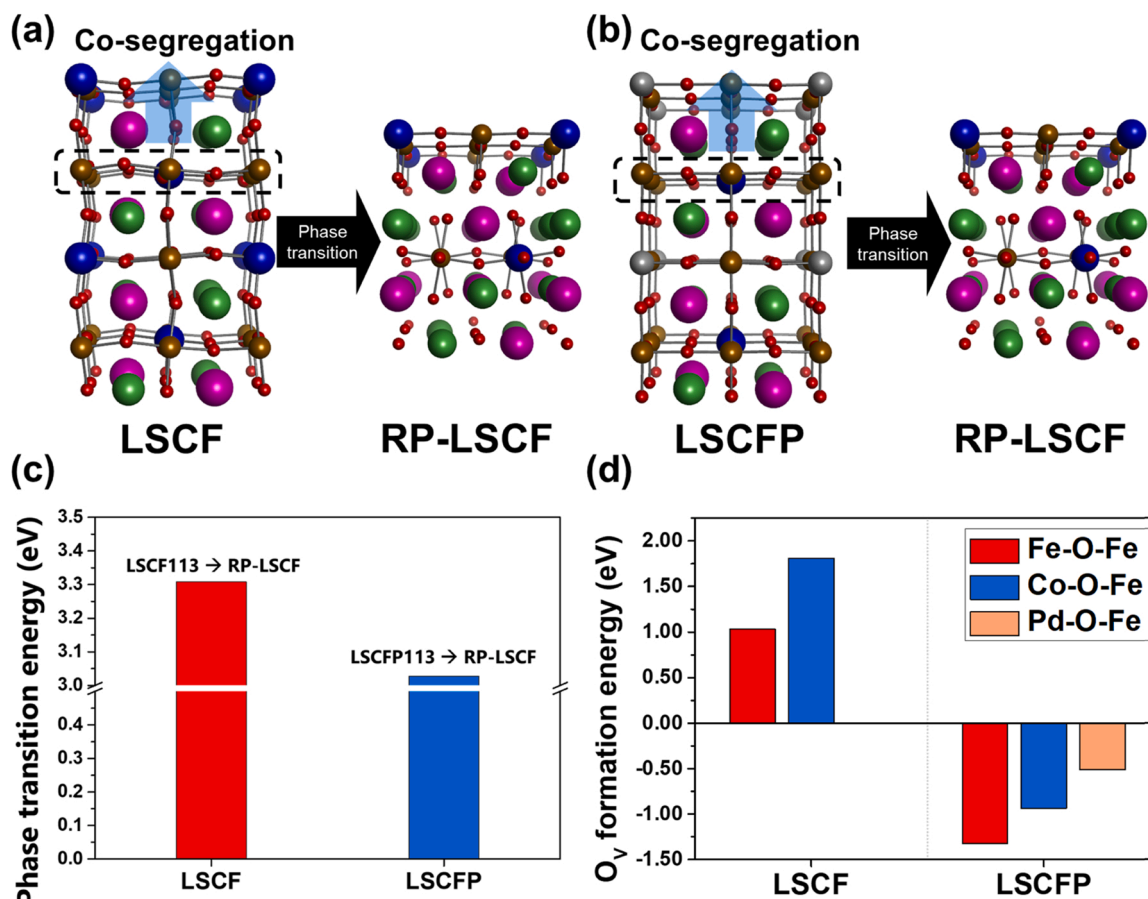

Fig. 4. DFT-optimized structures of (a) bulk LSCF (simple perovskite), RP-LSCF (RP phase), (b) and bulk LSCFP (simple perovskite). Blue, red, gray, brown, green, and purple spheres are Co, O, Pd, Fe, La, and Sr atoms, respectively. (c) Phase transition energies of LSCF and LSCFP perovskites to RP-LSCF, respectively. (d) Oxygen vacancy formation energies in the BO2 layer of bulk LSCF and LSCFP.
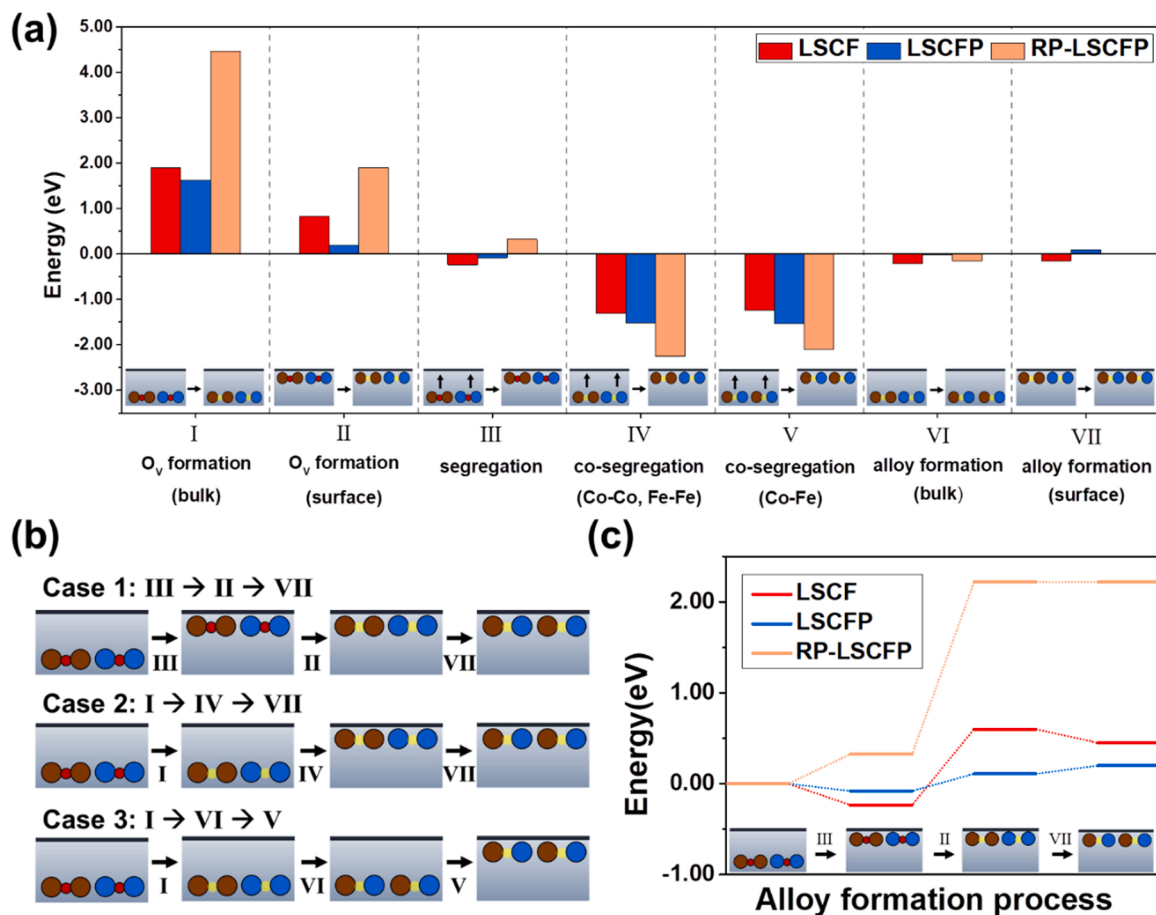
Fig. 5. (a) Seven key energetics required for the exsolution process of Co-Fe alloy on LSCF (red), LSCFP (blue), and RP-LSCFP (orange). (b) Three possible pathways for the exsolution of Co-Fe alloy based on the fundamental steps in (a). Brown, red, blue, yellow circle indicate Fe, Co, and oxygen atoms, and oxygen vacancies, respectively. (c) Energy diagram of case 1 for LSCF, LSCFP, and RP-LSCFP.

segregation energy of Co-O$_V$-Fe ($E_{co-segregation\_alloy}$), VI: bulk alloy formation energy ($E_{alloy-formation\_bulk}$), and VII: surface alloy formation energy ($E_{alloy-formation\_surface}$). With these energetics, it is possible to compare the energies required for B-cation segregation toward the support surface ($E_{segregation}$, $E_{co-segregation}$), metallic phase formation of the exsolved metal (E_{vf_bulk}, $E_{vf\_surface}$, $E_{co-segregation}$), and alloy metal formation ($E_{alloy-formation\_bulk}$, $E_{alloy-formation\_surface}$) [10,11]. A comparative study revealed that oxygen vacancy formation required the highest energy for the three surface models (Fig. 5a). In particular, E_{vf_bulk} was much higher than $E_{vf\_surface}$, implying that oxygen vacancy formation occurred more easily at the surface than in the bulk for all surface models.

Combining these key energetics (Fig. 5a), there are three possible exsolution pathways for the Co-Fe alloy (Fig. 5b). They are classified by the location at which oxygen vacancy formation and alloy formation occur. In case 1 [III→II→VII], B-cation segregation (M-O-M pair) occurs first, followed by the formation of oxygen vacancies at the surface. On the other hand, in case 2 [I→IV→VII] and 3 [I→VI→V], oxygen vacancy formation occurs first in the bulk, then co-segregation (M-O_{vac}-M pair) occurs. The difference between cases 2 and 3 is the location at which cation aggregation occurs to form a Co-Fe alloy. Among the three pathways, case 1 is thermodynamically preferred over cases 2 and 3 because E_{vf_bulk} in the latter cases is much higher than any other energy required for the fundamental steps of case 1 (Fig. 5a-b) on the three surface models. Therefore, case 1 was used to compare the exsolution trends of cubic LSCF and LSCFP perovskites, and RP-LSCFP (Fig. 5c), and rhombohedral LSCF and LSCFP perovskites (Fig. S9). Step II (surface vacancy formation) required the highest energy in the pathway for all five surface models. This is consistent with the result that $E_{vf\_surface}$ is

higher than $E_{segregation}$ and $E_{alloy-formation\_surface}$ (Fig. 5a). In cubic and rhombohedral perovskites, LSCFP required lower energy for step II than LSCF because Pd doping reduced the $E_{vf\_surface}$ of LSCFP more than that of LSCF. The required energy for step II was the highest for RP-LSCFP because $E_{vf\_surface}$ of RP-LSCFP increased drastically after the phase transition. As a result, the energy of the final state (exsolved Co-Fe alloy formed on the surface) was the lowest for LSCFP, indicating the easiest exsolution of Co-Fe alloy on LSCFP than LSCF. In addition, the highest final state energy of RP-LSCFP shows the difficulty of exsolution after the phase transition, which implies that the phase transition occurs after exsolution.

3.6. In-situ HR-XRD studies

To verify the DFT calculation results for the emergence of phase transition and exsolution in LSCFP, *in-situ* high-temperature XRD of LSCFP under 100% H$_2$ (with H$_2$O) was conducted in the temperature range of 30–850 °C. The resultant XRD patterns at different temperatures are shown on the left side of Fig. 6. The synthesized LSCFP maintained a rhombohedral perovskite structure from room temperature to 450 °C. However, as the temperature reached 550 °C, a Co-Fe alloy peak appeared at ~ 44°, indicating that the metal cations were exsolved from the perovskite lattice to the surface. At 700 °C, the LSCFP phase started to undergo phase transition from perovskite to RP while maintaining the exsolved Co-Fe metallic alloys. (Note that we observed a very minor peak (~ 44°) for metallic Pd (> 650 °C) that overlaps with one of the perovskite peaks; thus, it is not clear when the metallic Pd phase was formed.) Fig. 6 (right side) illustrates the schematics of the
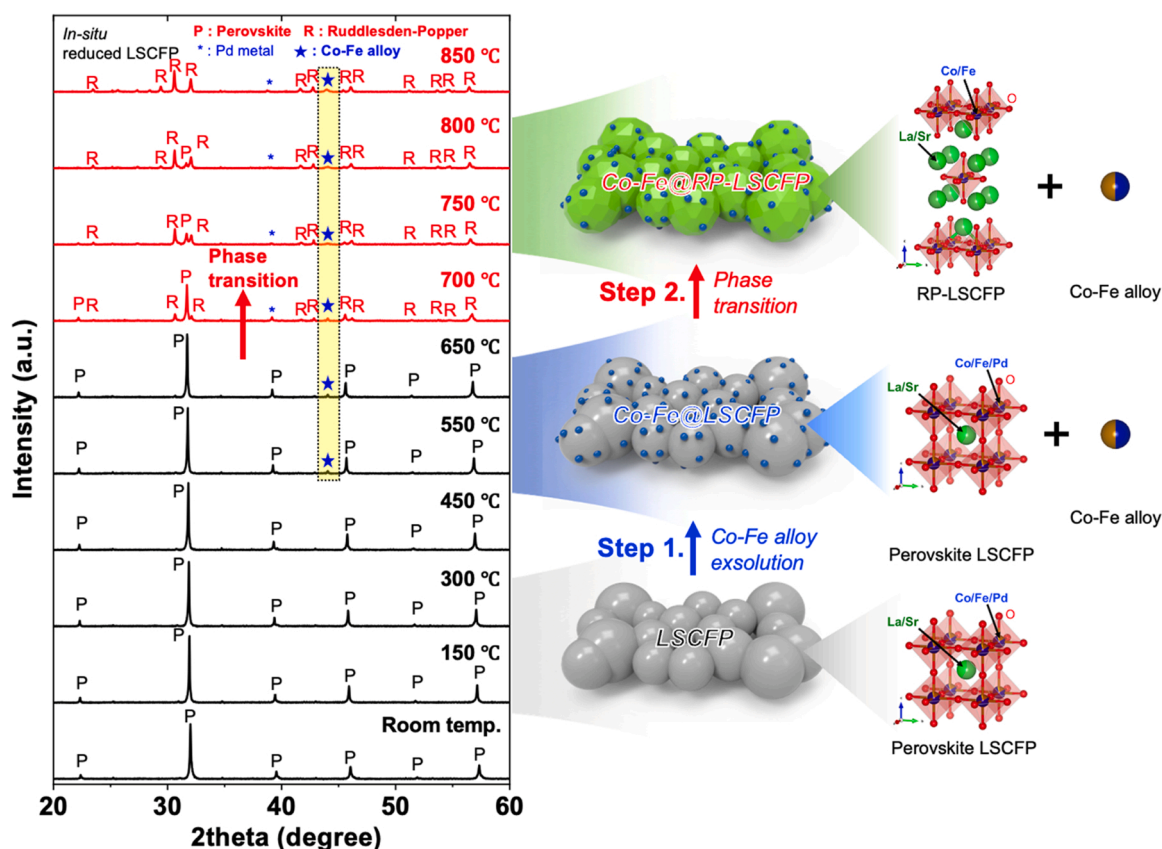
Fig. 6. *In-situ* XRD patterns and model of the surface morphology evolution of LSCFP under a reducing atmosphere.

surface morphologies with the corresponding atomic structures of LSCFP at different stages. This observation reveals that, as the temperature increases under the reducing condition, the Co-Fe nano-catalysts are *in-situ* exsolved on the LSCFP surface, followed by the phase transformation of the LSCFP bulk from the perovskite into the RP phase, as expected from the DFT calculations (Figs. 4 and 5).

3.7. Hydrogen oxidation reaction

Fig. 7a shows the impedance spectra of the LSCFP and LSCF electrodes on LSGM-electrolyte-symmetric cells measured at 750 °C using electrochemical impedance spectroscopy (EIS) under open-circuit conditions in H_2. To directly compare the electrode area specific resistances (ASRs) with different catalysts, we subtracted the ohmic resistance from the high-frequency intercept along with the real axis of each Nyquist plot. The difference between the high- and low-frequency intercepts at the real axis was estimated as the electrode ASR in a reducing atmosphere. The electrode ASR of LSCFP in H_2 at 750 °C (0.13 Ω·cm^2) was approximately five times lower than that of LSCF (0.60 Ω cm^2). This can be explained by the fact that, under reducing conditions, the *in-situ* exsolution of metallic nanocatalysts on completely phase-transformed RP-LSCFP significantly contributed to enhancing the electrocatalytic activity of the LSCFP fuel electrode during the HOR. Fig. 7b compares the electrode ASRs of the LSCFP and LSCF electrodes as a function of inverse temperature, indicating that the LSCFP electrode outperformed the LSCF electrode at all measured temperatures.

Fig. 7c shows the redox behavior of the LSCFP electrode monitored *in situ* by EIS measurements over 16 redox cycles (total 60 h). The inset of Fig. 7c displays a sequence of one redox cycle with an alternating atmosphere of H_2 and air at 750 °C with a flow rate of 200 ml min^{-1}. The resultant ASR of LSCFP in H_2 at 750 °C was initially 0.13 Ω·cm^2, increasing to 0.14 Ω·cm^2 after 16 redox cycles, indicating no

degradation of the catalytic activity of the LSCFP electrode. These results clearly demonstrate that the LSCFP fuel electrode has excellent redox stability (0.4% degradation rate) compared to recently reported perovskite-based fuel electrodes, such as $La_{0.8}Sr_{0.2}Cr_{0.8}Mn_{0.2}O_{3-\delta}$-$Gd_{0.1}Ce_{0.9}O_{1.95}$(GDC)-Ni (7.81% degradation rate),[35] $La_{0.85}Sr_{0.15}Cr_{0.9}Ni_{0.1}O_3$ (21.08% degradation rate),[36] and $SrGdNi_{0.2}Mn_{0.8}O_{4-\delta}$ (1.78% degradation rate) [8].

In addition, microstructural evolution of the LSCFP electrode during a redox cycle, consisting of oxidation, reduction, and re-oxidation steps, was analyzed by SEM (Fig. 7d). Initially, no particles were observed on the surface of LSCFP (left in Fig. 7d), while it is clearly shown that a significant number of exsolved nanoparticles were observed on the LSCFP surface after exposure to H_2 for 2 h (middle of Fig. 7d). After subsequent re-oxidation of the reduced LSCFP fuel electrode, however, the exsolved nanoparticles on the surface disappeared (right in Fig. 7d). This result suggests that the metallic nanoparticles dissolved in the host LSCFP lattice in an oxidizing atmosphere, effectively preventing agglomeration of the nanoparticles.

3.8. Electrochemical performances in FC and EC modes

Fig. 8a shows the I-V-P characteristics of LSCFP|LSGM|LSCF-GDC and LSCF|LSGM|LSCF-GDC cells were measured at 850 °C. The measured open circuit voltage values were approximately 1.1 V; this is the ideal theoretical value derived by the Nernst equation at two cells, indicating a good separation between the anodic and cathodic gases due to the highly dense electrolyte. The SOC with the LSCFP fuel electrode yielded an MPD of 2.00 W cm^{-2}, which was ~ 110% higher than that of the undoped LSCF cell (0.94 W cm^{-2}). Considering the identical structures of both cells, except for the fuel electrode material (Fig. S10), the LSCFP fuel electrode could have a primary impact on the enhancement of the FC performance. Fig. 8b displays Nyquist and Bode plots of EIS
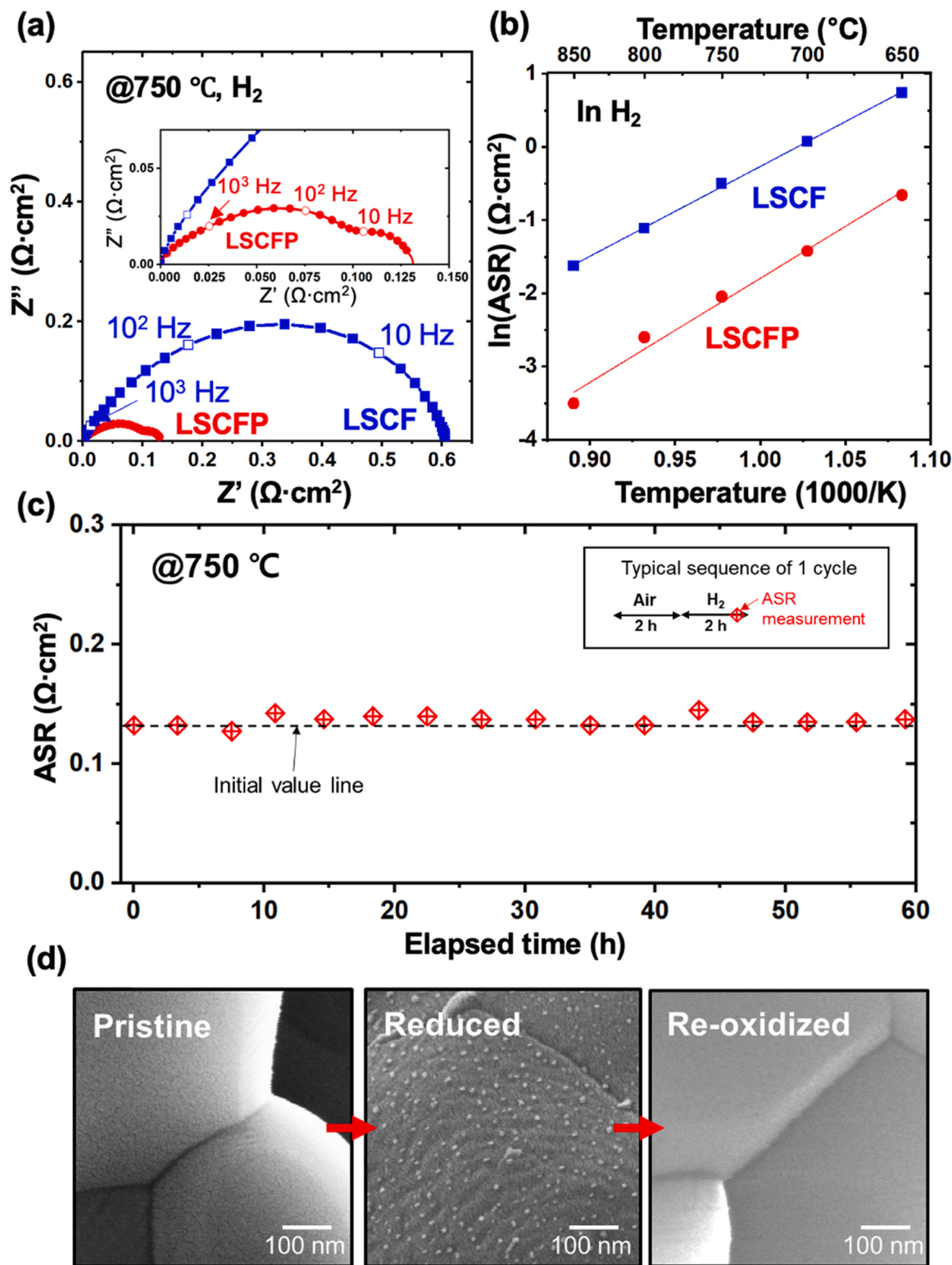
Fig. 7. (a) Nyquist plot of electrochemical impedance data of symmetrical cells LSCFP|LSGM|LSCFP and LSCF|LSGM|LSCF measured in H_2 under open-circuit voltage at 750 °C. (b) Arrhenius plots for ASR of LSCFP and LSCF in H_2. (c) Cyclic stability of LSCFP|LSGM|LSCFP at 750 °C over 16 cycles, in which the fuel electrode gas was switched between H_2 and air. (d) Cross-sectional SEM images of LSCFP anode during a redox cycle (oxidation → reduction → reoxidation).

data from both cells. Their corresponding fitting results using an equivalent circuit (Fig. S11) are overlaid in Fig. 8b. High frequency ($\sim 10^4$ Hz) responses remained constant regardless of the two anode types. In contrast, the middle frequency ($\sim 10^3$ Hz) and low frequency (~ 1 Hz) responses can be assigned to primary anode and secondary anode responses, respectively. Thus, the distinguishable frequency peaks of LSCF and LSCFP can be explained by the difference in charge transfer by hydrogen dissociation and the response to molecular hydrogen adsorption [37]. To closely elucidate which sub-processes affected the HOR response, we conducted a distribution of relaxation
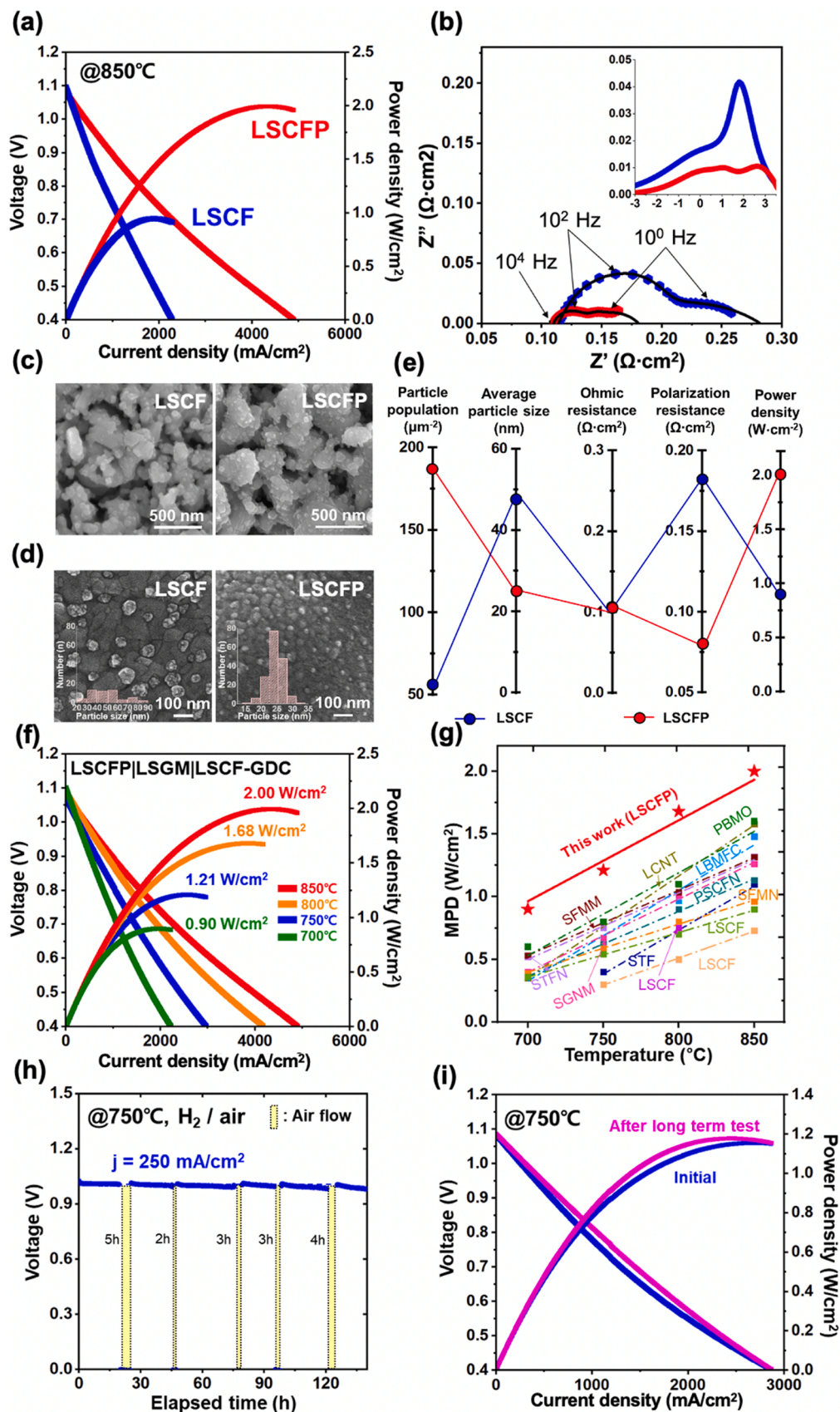
Fig. 8. (a) Comparison I-V-P performance between LSCF and LSCFP cell at 850 °C. (b) Nyquist plot of LSCF and LSCFP cells at 850 °C; inset image is Bode plot corresponding to Nyquist plot. Surface SEM image of LSCF and LSCFP cell after FC test: (c) low resolution and (d) high resolution. (e) Various characteristics of the samples shown in (a-d), plotted in a parallel coordinate system. (f) Cell voltages and power densities *versus* current densities of LSCFP||LSGM|LSCF-GDC at 700–850 °C. (g) Comparison of the MPDs at various temperatures. (h) Redox stability evaluation under a constant current density of 250 mA cm^{-2} at 750 °C under $H_2 - 3\%$ H_2O and air as the fuel and oxidant, respectively; the five redox cycles were conducted with various oxidation times. (i) I-V-P performance of LSCFP fuel electrode-based single cell at 750 °C before and after the test.

time (DRT) analysis on the electrochemical impedance spectroscopy data of LSCFP|LSGM|LSCF-GDC and LSCF|LSGM|LSCF-GDC SOCs (Fig. S12a-b). In both cells, 4 peaks were observed; the 2nd peak ($10^3 \sim 10^2$ Hz), which is the rate-determining reaction in the LSCF electrode, sharply decreased in the LSCFP electrode. This peak is associated with the charge transfer region of the anode, and it can be expected that the HOR response with the LSCFP electrode was rapidly improved by Co-Fe exsolution [38,39]. Of course, although nanoscale Pd particles were also actually observed, the population of it was too low compared to the amount of Co-Fe, and the most apparent difference between LSCF and LSCFP was the activation energy of Co-Fe alloy nanocatalyst exsolution, which was lower for LSCFP due to the Pd doping. (Fig. 5c) Consistently, the polarization resistance of LSCFP cell ($0.07 \ \Omega \cdot cm^2$) exhibited the 61% lower polarization resistance as compared to that of LSCF cell ($0.18 \ \Omega \cdot cm^2$), while the ohmic resistance at 850 °C was similar to $0.11 \ \Omega \cdot cm^2$ for both cells. Fig. 8c shows the microstructural analysis of the LSCF and LSCFP electrodes after the FC test, indicating similarly porous structures with exsolved nanoparticles. However, magnified images in higher resolution (Fig. 8d) revealed that nanoparticles on the LSCFP surface had significantly smaller size and higher population than that of the LSCF sample. Insets of Fig. 8d shows plots of the number of particles as a function of particle size on the surface of LSCF and LSCFP, which were analyzed by an imaging software (ImageJ) as shown in Fig. S13. The size of exsolved nanoparticles of the LSCF was widely distributed between 20 and 90 nm with average particle size of 49 nm, whereas LSCFP had much smaller nanoparticles at average particle size of ~ 25 nm with more uniform distribution between 15 and 35 nm. As a result, the particle density on the surface reduced LSCFP ($170 \ \mu m^{-2}$) was ~ 3.3 times higher than that of LSCF ($52 \ \mu m^{-2}$). Fig. 8e shows the summary of microstructural properties of exsolved nanoparticles (Fig. 8d) and electrochemical performances at 850 °C (Fig. 8a-b) of LSCF and LSCFP cells. Compared to LSCF, nanoparticles population increase (> 3 times from 52 to $170 \ \mu m^{-2}$) in LSCFP is inversely correlated to polarization resistance decrease in LSCFP (1/3 from 0.18 to $0.07 \ \Omega \cdot cm^2$), which was reasonably reflected to MPD increase (from $0.94 \ W \ cm^{-2}$ for LSCF to $2 \ W \ cm^{-2}$ for LSCFP). Thus, these results suggest that the highly reducible Pd doping into LSCF promoted to form finely dispersed nanoparticles *via* facilitating nucleation of metallic nanoparticles at lower temperature, and these nanocatalysts enhanced HOR activity of the LSCFP electrode in the FC operation. To confirm this theory, we reduced LSCF and LSCFP electrodes at lower temperature of 700 °C and observed the microstructural morphologies (Fig. S14). It clearly shows that the reduced LSCFP sample had a plenty of exsolved nanoparticles, while there were no apparent exsolved nanoparticles on the reduced LSCF at 700 °C.

Fig. 8 f shows temperature dependent I-V-P curves of the SOC with the LSCFP electrode in the temperature range of 700–850 °C. The MPD values of the LSCFP cell were extraordinarily high as 2.00, 1.68, 1.21, and $0.90 \ W \ cm^{-2}$ at 850, 800, 750, and 700 °C, respectively. Fig. 8g (and Table 3) compares the MPDs of SOCs with various perovskite-based fuel electrodes from this study and in the literature as a function of temperature [4,8,12,19,29,40–45]. As shown in this figure, our LSCFP electrode significantly outperformed recently reported state-of-the-art ceramic fuel electrodes in the FC mode at all test temperatures. For example, at 850 °C, although the oxygen electrode and the electrolyte were similar for all three cells, the SOC with LSCFP ($2.00 \ W \ cm^{-2}$) exhibited 45% and 52% higher performance in MPD compared to SOCs with perovskite $Sr_{0.95}(Ti_{0.3}Fe_{0.63}Ni_{0.07})O_{3-\delta}$ ($1.11 \ W \ cm^{-2}$) [43] and RP phase $SrGdNi_{0.2}Mn_{0.8}O_{4-\delta}$ ($1.13 \ W \ cm^{-2}$) fuel electrodes, respectively [8]. Subsequent to the initial I-V-P characteristics, the redox cycling durability of the SOC with the LSCFP electrode was investigated. Fig. 8h shows the short-term performance at 750 °C for an LSCFP cell driven under a constant current density of $250 \ mA \ cm^{-2}$ with irregular switching gas conditions between H_2 and air at the fuel electrode. During the redox operation, the voltage of the LSCFP cell dropped to ~ 0 V upon oxidation in air; upon reduction in H_2, the voltage was restored to the initial value and stably maintained. Fig. 8i directly compares the I-V-P curves of the LSCFP SOC before and after the redox operation test, exhibiting almost identical I-V-P behavior in both cases (even slightly higher after redox cycling tests; $1.17 \ W \ cm^{-2}$ for initial measurement *vs.* $1.19 \ W \ cm^{-2}$ after the redox operation test). Thus, these results demonstrate the excellent redox and long-term stability of the LSCFP electrode with exsolved Co-Fe alloy nanocatalysts.

Fig. 9a shows the I-V plots of an LSCFP fuel electrode-based cell, which were consecutively measured in EC and FC modes at temperatures from 700° to 850°C over a voltage range of 0.5–1.5 V. The negative current density indicates that the SOC is in the EC mode, while the positive current density indicates that the SOC is in the FC mode. The feed gases were fixed with H_2/H_2O (50:50 ratio) in the fuel electrode, and dry air in the oxygen electrode. At 1.3 V (near the thermo-neutral voltage for steam electrolysis), the current densities of LSCFP cell at 700, 750, 800, and 850 °C were − 0.77, − 1.16, − 1.62, and − 2.23 A cm^{-2}, respectively. Because the electricity applied to the cell at thermo-neutral voltage (~1.3 V) has the equivalent energy required for steam electrolysis, the efficiency of electro-hydrogen conversion is assumed to be 100%. In this case, the rate of hydrogen production (ΔN_{H_2}, ml^{-1} cm^{-2}) corresponding to the current density can be derived by the following equation:

Table 3
Comparison of the performance of various perovskite-based fuel electrode-employed solid oxide fuel cells.

Fuel electrode	Electrolyte	Oxygen electrode	MPD (W/cm^2)				Ref.
			850 °C	800 °C	750 °C	700 °C	
LSCFP	LSGM	LSCF[12]-GDC	2.00	1.68	1.21	0.90	this work
LSCF	LSGM	LSCF[12]-GDC	0.94	0.72	0.52	0.31	this work
LSCF[12]-GDC	LSGM	LSCF[12]-GDC	0.73	0.50	0.30	–	[12]
LSCF/Ni-YSZ	YSZ	LSM[6]-YSZ	–	0.75	–	–	[19]
PBMO1	LDC[2]/LSGM	NBSCF[3]-GDC	1.70	1.40	1.10	0.70	[4]
LCNT[4]	ScSZ[5]	LSM[6]–ScSZ	1.60	1.10	0.80	0.35	[40]
LBMFC[7]	LDC/LSGM	BSCF[8]	1.48	0.97	0.65	0.38	[41]
SFMM[9]	LSGM	LSCF[10]	1.32	1.04	0.80	0.53	[42]
STFN[11]	LDC/LSGM	LSCF[12]-GDC	1.32	1.00	0.75	0.52	[43]
SGNM[13]	LSGM	LSCF[12]-GDC	1.26	1.01	0.67	0.40	[8]
PSCFN[14]	YSZ	BCFN[15]	1.13	0.90	0.62	0.36	[44]
STF[16]	LDC/LSGM	STF	1.10	0.70	0.40	–	[45]
SFMN[17]	LDC/LSGM	LSCF[10]	0.96	0.80	0.59	0.39	[29]

[1]PBMO: $Pr_{0.5}Ba_{0.5}MnO_3$, [2]LDC: $La_{0.4}Ce_{0.6}O_{2-\delta}$, [3]NBSCF: $NdBa_{0.5}Sr_{0.5}Co_{1.5}Fe_{0.5}O_{5+\delta}$, [4]LCNT: $La_{0.43}Ca_{0.37}Ni_{0.06}Ti_{0.94}O_3$, [5]ScSZ: $Zr_{0.89}Sc_{0.1}Ce_{0.01}O_{2-\gamma}$, [6]LSM: $La_{0.8}Sr_{0.2}MnO_{3+\delta}$,LBMFC: $La_{0.5}Ba_{0.5}Mn_{0.8}Fe_{0.1}Co_{0.1}O_{3-\delta}$, [8]BSCF: $Ba_{0.5}Sr_{0.5}Co_{0.8}Fe_{0.2}O_{3-\delta}$, [9]SFMM: $Sr_2FeMo_{2/3}Mg_{1/3}O_{6-\delta}$, [10]LSCF: $La_{0.58}Sr_{0.4}Fe_{0.8}Co_{0.2}O_{3-\delta}$, [11]STFN: $Sr_{0.95}(Ti_{0.3}Fe_{0.63}Ni_{0.07})O_{3-\delta}$, [12]LSCF: $La_{0.6}Sr_{0.4}Fe_{0.8}Co_{0.2}O_{3-\delta}$, [13]SGNM: $SrGdNi_{0.2}Mn_{0.8}O_{4-\delta}$, [14]PSCFN: $Pr_{0.8}Sr_{1.2}(Co, \ Fe)_{0.8}Nb_{0.2}O_{4+\delta}$, [15]BCFN: $Ba_{0.9}Co_{0.7}Fe_{0.2}Nb_{0.1}O_{3-\delta}$, [16]STF: $SrTi_{0.3}Fe_{0.7}O_{3-\delta}$, [17]SFMN: $Sr_2FeMo_{0.65}Ni_{0.35}O_{6-\delta}$.
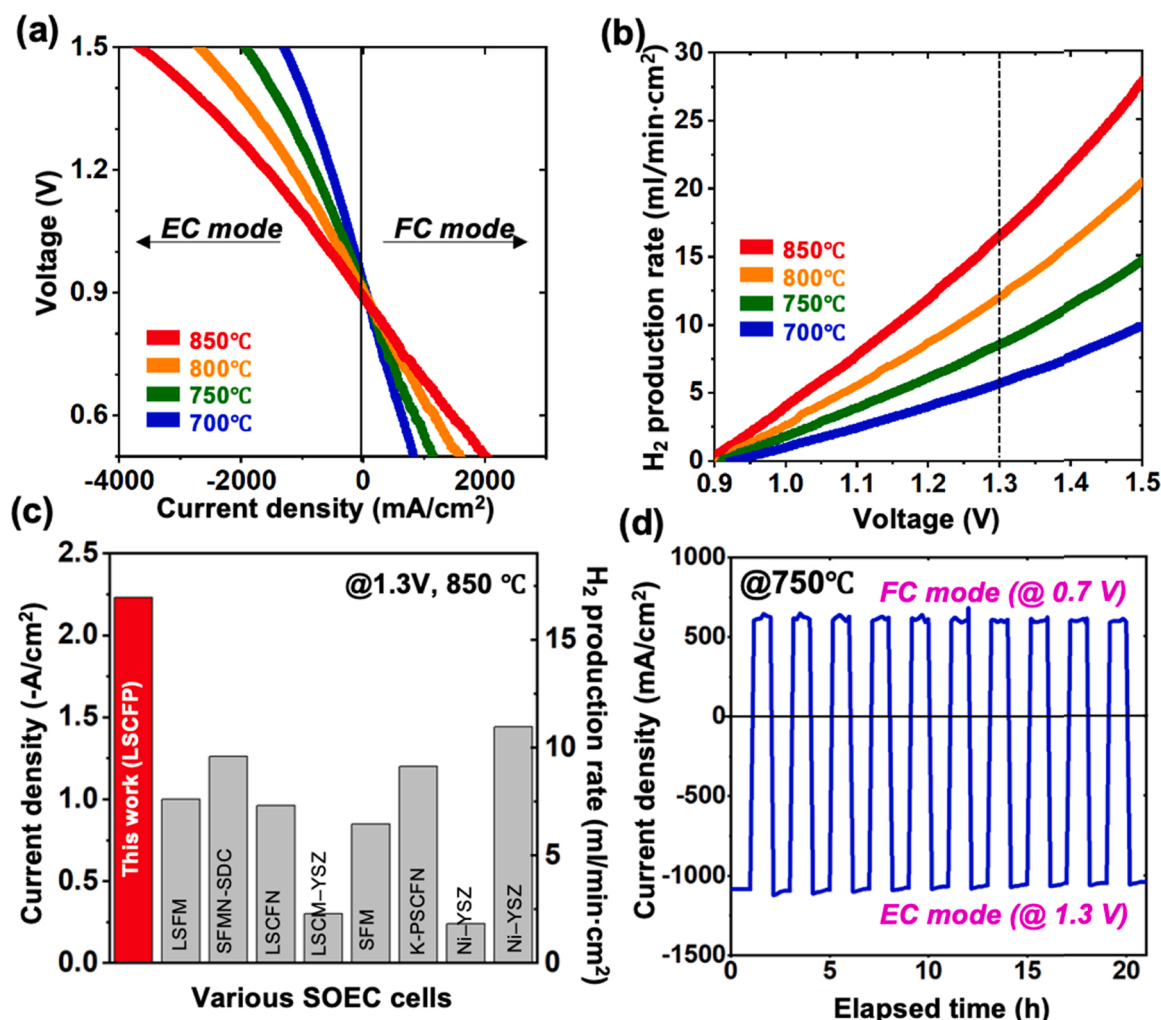
Fig. 9. (a) Electrolysis and fuel cell performance of LSCFP|LSGM|LSCF-GDC with 50% H_2O/H_2 gas from 700 to 850 °C. (b) H_2 production rate of LSCFP SOC under EC mode. (c) Comparison of the current density with H_2 production rate at 1.3 V of the present work and other literature studies. (d) Continuous cyclic operation between EC (@ 1.3 V) and FC mode (@ 0.7 V) at 750 °C.

$$\Delta N_{H_2} = \frac{-I}{2F} \qquad\qquad (6)$$

where I is the current density (A) and F is the Faraday constant (C). Based on Eq. (1), the estimated ΔN_{H_2} of the LSCFP cell was displayed as a function of temperature (Fig. 9b). At 1.3 V, the ΔN_{H_2} values of the cell at 700, 750, 800, and 850 °C were 5.73, 8.63, 12.07, and 16.51 ml min^{-1} cm^{-2}, respectively. As the temperature increased, ΔN_{H_2} increased. Fig. 9c and Table 4 compare the electrolysis performance of the LSCFP cell with various fuel electrode-employing cells in the literature, showing the remarkable electrolysis performance of the LSCFP fuel electrode cell at 850 °C [46–53]. Furthermore, Fig. 9d shows the *in-situ* monitored current density behavior under an alternating voltage between 0.7 V (FC mode) and 1.3 V (EC mode) at 750 °C for 21 h. No significant performance deterioration was observed during ten reversible cycles, suggesting good reversibility of the LSCFP fuel electrode for both HOR and HER activity.

4. Conclusions

In this study, we developed a novel fuel electrode using a Pd-doped LSCF perovskite for reversible SOCs. Crystallographic analysis revealed that upon reduction in H_2 at 700 °C, the cubic perovskite phase of LSCFP was completely transformed into a single RP phase with a bimetallic Co-Fe phase. In addition, the oxidation states of the B-site elements of LSCFP

after reduction significantly decreased compared to that of LSCF, suggesting that Pd doping in the perovskite LSCF lattice effectively promoted the reducibility of the B-site element into metallic states under H_2 conditions, which was consistent with the *in-situ* H_2-TPR analysis. Moreover, HR-TEM-EDS mapping revealed that the exsolved Co-Fe bimetallic nanocatalysts were uniformly distributed on the surface of the RP LSCFP. DFT calculations showed that Pd doping dramatically reduced the oxygen vacancy formation energy of LSCF, effectively accelerating the phase transition under reduction conditions. Furthermore, a comparative study of the oxygen vacancy formation energy, segregation energy, and co-segregation energy verified that Co-Fe co-exsolution was governed by the oxygen vacancy formation step rather than the cation segregation or co-segregation step. Because the oxygen vacancy formation energy increased significantly after the phase transition, the bimetallic exsolution should occur prior to the phase transition. This interesting theory on the order of exsolution and phase transition was experimentally demonstrated using *in-situ* HT-XRD.

The LSCFP electrode on the LSGM electrolyte exhibited five times lower ASR (0.12 Ω cm^2) in H_2 at 750 °C compared to that of un-doped LSCF (0.60 Ω cm^2), with remarkable redox stability over 16 cycles due to reversible exsolution and dissolution behavior of the Co-Fe bimetallic phase in LSCFP. Finally, the electrochemical performance of the SOC with the LSCFP fuel electrode in reversible operations was extraordinary in both FC (2.00 W cm^{-2} in MPD at 850 °C) and EC (2.23 A/cm^2 at 1.3 V

Table 4

Comparison of current density (@850 °C) of various solid oxide electrolysis cells.

Fuel electrode	Electrolyte	Oxygen electrode	Fuel condition	Current density / -A cm^{-2}(at 1.3 V, 850 °C)	Ref.
LSCFP	LSGM	LSCF-GDC	50% H$_2$O / 50% H$_2$	2.23	this work
LSFM[1]	LSGM	LSFM[1]	20% H$_2$O / 80% H$_2$	1.00	[46]
SFMN[2]-SDC[3]	LSGM	LSCF-SDC[3]	42% H$_2$O / 58% H$_2$	1.26	[47]
LSCFN[4]	YSZ	SSNC[5]	50% H$_2$O / 50% H$_2$	0.96	[48]
LSCM[6]-YSZ	YSZ	LSM[7]-YSZ	60% H$_2$O / 40% H$_2$	0.30	[49]
SFM[8]	LSGM	SFM[8]	60% H$_2$O / 40% H$_2$	0.85	[50]
K-PSCFN	LSGM	BCFN	40% H$_2$O / 60% H$_2$	1.20	[51]
Ni-YSZ	YSZ	LSM[9]-YSZ	60% H$_2$O /40% H$_2$	0.24	[52]
Ni-YSZ	YSZ	NBCCF[10]-GDC	50% H$_2$O / 50% H$_2$	1.44	[53]

[1]LSFM: La$_{0.5}$Sr$_{0.5}$Fe$_{0.9}$Mo$_{0.1}$O$_{3-\delta}$, [2]SFMN: Sr$_2$Fe$_{1.3}$Ni$_{0.2}$Mo$_{0.5}$O$_6$, [3]SDC: Sm$_{0.4}$Ce$_{0.6}$O$_{2-\delta}$, [4]LSCFN: La$_{0.4}$Sr$_{0.55}$Co$_{0.2}$Fe$_{0.6}$Nb$_{0.2}$O$_3$, [5]SSNC: SrSc$_{0.175}$Nb$_{0.025}$Co$_{0.8}$O$_{3-\delta}$, [6]LSCM: La$_{0.75}$Sr$_{0.25}$Cr$_{0.5}$Mn$_{0.5}$O$_{3-\delta}$, [7]LSM: La$_{0.8}$Sr$_{0.2}$MnO$_3$ [8]SFM: Sr$_2$Fe$_{1.5}$Mo$_{0.5}$O$_{6-\delta}$, [9]LSM: (La$_{0.75}$Sr$_{0.25}$)$_{0.95}$MnO$_3$, [10]NBCCF: NdBa$_{0.5}$Ca$_{0.5}$Co$_{1.5}$Fe$_{0.5}$O$_{5+\delta}$.

at 850 °C) modes, which is one of the best values to date. Thus, our results comprehensively demonstrate that LSCFP with simultaneous phase transition and bimetallic exsolution in H$_2$ is highly promising as a robust bifunctional electrocatalyst for reversible SOC applications.

Author contributions

Kyeong Joon Kim, Kyung Taek Bae, and Jong Jun Lee performed the experiments and analyzed the data; Chaesung Lim, Jeong Woo Han carried out the *ab initio* calculations; Mi Young Oh; Hyung Jun Kim, Jong Jun Lee, and Hyunmin Kim contributed experimental materials; Guntae Kim, Tae Ho Shin, Jeong Woo Han, and Kang Taek Lee commented on the manuscript; Kang Taek Lee conceived of the study, coordinated the study, and revised the draft of the manuscript. All authors participated in writing a manuscript and gave final approval for publication and agree to be held accountable for the work performed therein.

Declaration of Competing Interest

The authors declare that they have no known competing financial interests or personal relationships that could have appeared to influence the work reported in this paper.

Acknowledgment

Appendix A. Supplementary material

Supplementary data associated with this article can be found in the online version at doi:10.1016/j.apcatb.2022.121517.

References

[1] D. Kim, J.W. Park, M.S. Chae, I. Jeong, J.H. Park, K.J. Kim, J.J. Lee, C. Jung, C.-W. Lee, S.-T. Hong, An efficient and robust lanthanum strontium cobalt ferrite catalysts as a bifunctional oxygen electrode for reversible solid oxide cells, J. Mater. Chem. A (2021).

[2] M. Keane, H. Fan, M. Han, P. Singh, Role of initial microstructure on nickel-YSZ cathode degradation in solid oxide electrolysis cells, Int. J. Hydrog. Energy 39 (2014) 18718–18726.

[3] B. Mewafy, F. Paloukis, K.M. Papazisi, S.P. Balomenou, W. Luo, D. Teschner, O. Joubert, A. Le Gal La Salle, D.K. Niakolas, S. Zafeiratos, Influence of surface state on the electrochemical performance of nickel-based cermet electrodes during steam electrolysis, ACS Appl. Energy Mater. 2 (2019) 7045–7055.

[4] S. Sengodan, S. Choi, A. Jun, T.H. Shin, Y.-W. Ju, H.Y. Jeong, J. Shin, J.T. Irvine, G. Kim, Layered oxygen-deficient double perovskite as an efficient and stable anode for direct hydrocarbon solid oxide fuel cells, Nat. Mater. 14 (2015) 205–209.

[5] W. Kobsiriphat, B. Madsen, Y. Wang, L. Marks, S.A. Barnett, La0. 8Sr0. 2Cr1−xRuxO3−δ–Gd0. 1Ce0. 9O1. 95 solid oxide fuel cell anodes: Ru precipitation and electrochemical performance, Solid State Ion. 180 (2009) 257–264.

[6] J.T. Irvine, P. Connor, Solid Oxide Fuels Cells: Facts and Figures, Springer, 2013.

[7] Y.S. Chung, T. Kim, T.H. Shin, H. Yoon, S. Park, N.M. Sammes, W.B. Kim, J. S. Chung, In situ preparation of a La1.2Sr0.8Mn0.4Fe0.6O4 Ruddlesden–Popper phase with exsolved Fe nanoparticles as an anode for SOFCs, J. Mater. Chem. A 5 (2017) 6437–6446.

[8] K.J. Kim, M.K. Rath, H.H. Kwak, H.J. Kim, J.W. Han, S.-T. Hong, K.T. Lee, A highly active and redox-stable SrGdNi0. 2Mn0. 8O4±δ anode with in situ exsolution of nanocatalysts, ACS Catal. (9) (2019) 1172–1182.

[9] D. Neagu, G. Tsekouras, D.N. Miller, H. Ménard, J.T. Irvine, In situ growth of nanoparticles through control of non-stoichiometry, Nat. Chem. 5 (2013) 916–923.

[10] O. Kwon, K. Kim, S. Joo, H.Y. Jeong, J. Shin, J.W. Han, S. Sengodan, G. Kim, Self-assembled alloy nanoparticles in a layered perovskite as a fuel oxidation catalyst for solid oxide fuel cells, J. Mater. Chem. A 6 (2018) 15947–15953.

[11] O. Kwon, S. Sengodan, K. Kim, G. Kim, H.Y. Jeong, J. Shin, Y.W. Ju, J.W. Han, G. Kim, Exsolution trends and co-segregation aspects of self-grown catalyst nanoparticles in perovskites, Nat. Commun. 8 (2017) 15967.

[12] S. Park, H. Han, J. Choi, S. Lee, M. Park, W.B. Kim, Ruddlesden–Popper oxide (La0. 6Sr0. 4) 2 (Co, Fe) O4 with exsolved CoFe nanoparticles for a solid oxide fuel cell anode catalyst, Energy Technol. (2021) 2100116.

[13] J. Hwang, R.R. Rao, L. Giordano, Y. Katayama, Y. Yu, Y. Shao-Horn, Perovskites in catalysis and electrocatalysis, Science 358 (2017) 751–756.

[14] G. Kresse, J. Hafner, Norm-conserving and ultrasoft pseudopotentials for first-row and transition elements, J. Phys. Condens. Matter 6 (1994) 8245.

[15] D. Sholl, J.A. Steckel, Density Functional Theory: A Practical Introduction, John Wiley & Sons, 2011.

[16] J.P. Perdew, K. Burke, M. Ernzerhof, Generalized gradient approximation made simple, Phys. Rev. Lett. 77 (1996) 3865.

[17] B. Bouadjemi, S. Bentata, A. Abbad, W. Benstaali, B. Bouhafs, Half-metallic ferromagnetism in PrMnO3 perovskite from first principles calculations, Solid State Commun. 168 (2013) 6–10.

[18] H.J. Monkhorst, J.D. Pack, Special points for Brillouin-zone integrations, Phys. Rev. B 13 (1976) 5188.

[19] H. Chang, H. Chen, Z. Shao, J. Shi, J. Bai, S.-D. Li, In situ fabrication of (Sr, La) FeO 4 with CoFe alloy nanoparticles as an independent catalyst layer for direct methane-based solid oxide fuel cells with a nickel cermet anode, J. Mater. Chem. A 4 (2016) 13997–14007.

[20] S.-W. Zhang, B.-S. Yin, Y.-Z. Luo, L. Shen, B.-S. Tang, Z. Kou, X. Liu, D.-M. Gu, Z.-B. Wang, H. Gong, Fabrication and theoretical investigation of cobaltosic sulfide nanosheets for flexible aqueous Zn/Co batteries, Nano Energy 68 (2020), 104314.

[21] X. Li, S. Ding, X. Xiao, J. Shao, J. Wei, H. Pang, Y. Yu, N, S co-doped 3D mesoporous carbon–Co 3 Si 2 O 5 (OH) 4 architectures for high-performance flexible pseudo-solid-state supercapacitors, J. Mater. Chem. A 5 (2017) 12774–12781.

[22] Z. Zhao, C. Gao, K. Ma, Y. Lu, Pyrolysis derived helically nitrogen-doped carbon nanotubes with uniform cobalt for high performance oxygen reduction, Appl. Surf. Sci. 504 (2020), 144380.

[23] H. He, N. Qian, N. Wang, Magnetic CoFe2O4 films with controllable dendritic arrays by a combined method of electrodeposition and anode activation, CrystEngComm 17 (2015) 1667–1672.

[24] C. Kuivila, J. Butt, P.C. Stair, Characterization of surface species on iron synthesis catalysts by X-ray photoelectron spectroscopy, Appl. Surf. Sci. 32 (1988) 99–121.

[25] J. Sun, P. Zan, X. Yang, L. Ye, L. Zhao, Room-temperature synthesis of Fe3O4/Fe-carbon nanocomposites with Fe-carbon double conductive network as supercapacitor, Electrochim. Acta 215 (2016) 483–491.

[26] Y. Yazawa, H. Yoshida, N. Takagi, S.-i Komai, A. Satsuma, T. Hattori, Oxidation state of palladium as a factor controlling catalytic activity of Pd/SiO2–Al2O3 in propane combustion, Appl. Catal. B Environ. 19 (1998) 261–266.

[27] S. Lee, J.-M. Chung, Direct synthesis of H2O2 over acid-treated Pd/C catalyst derived from a Pd-Co core-shell structure, Catal. Today 352 (2020) 270–278.

[28] J.H. Kim, S.-W. Baek, C. Lee, K. Park, J. Bae, Performance analysis of cobalt-based cathode materials for solid oxide fuel cell, Solid State Ion. 179 (2008) 1490–1496.

[29] Z. Du, H. Zhao, S. Yi, Q. Xia, Y. Gong, Y. Zhang, X. Cheng, Y. Li, L. Gu, K. Swierczek, High-performance anode material Sr2FeMo0.65Ni0.35O6-delta with in situ exsolved nanoparticle catalyst, ACS Nano 10 (2016) 8660–8669.

[30] F. Puleo, L.F. Liotta, V. La Parola, D. Banerjee, A. Martorana, A. Longo, Palladium local structure of La 1− x Sr x Co 1− y Fe y− 0.03 Pd 0.03 O 3− δ perovskites synthesized using a one pot citrate method, Phys. Chem. Chem. Phys. 16 (2014) 22677–22686.

[31] L. Wang, J. Chen, H. Watanabe, Y. Xu, M. Tamura, Y. Nakagawa, K. Tomishige, Catalytic performance and characterization of Co–Fe bcc alloy nanoparticles

prepared from hydrotalcite-like precursors in the steam gasification of biomass-derived tar, Appl. Catal. B Environ. 160 (2014) 701–715.

[32] B. Levasseur, S. Kaliaguine, Methanol oxidation on LaBO3 (B= Co, Mn, Fe) perovskite-type catalysts prepared by reactive grinding, Appl. Catal. A Gen. 343 (2008) 29–38.

[33] Y.-F. Sun, J.-H. Li, L. Cui, B. Hua, S.-H. Cui, J. Li, J.-L. Luo, A-site-deficiency facilitated in situ growth of bimetallic Ni–Fe nano-alloys: a novel coking-tolerant fuel cell anode catalyst, Nanoscale 7 (2015) 11173–11181.

[34] C. Chen, F. Ciucci, Designing Fe-based oxygen catalysts by density functional theory calculations, Chem. Mater. 28 (2016) 7058–7065.

[35] J. Liu, B.D. Madsen, Z. Ji, S.A. Barnett, A fuel-flexible ceramic-based anode for solid oxide fuel cells, Electrochem. Solid State Lett. 5 (2002) A122.

[36] V.B. Vert, F.V. Melo, L. Navarrete, J.M. Serra, Redox stability and electrochemical study of nickel doped chromites as anodes for H2/CH4-fueled solid oxide fuel cells, Appl. Catal. B Environ. 115 (2012) 346–356.

[37] Y. Zhang, H. Zhao, Z. Du, K. Świerczek, Y. Li, High-performance SmBaMn2O5+ δ electrode for symmetrical solid oxide fuel cell, Chem. Mater. 31 (2019) 3784–3793.

[38] A. Leonide, V. Sonn, A. Weber, E. Ivers-Tiffée, Evaluation and modeling of the cell resistance in anode-supported solid oxide fuel cells, J. Electrochem. Soc. 155 (2007) B36.

[39] J.H. Park, H.-N. Im, K.T. Lee, Understanding redox cycling behavior of Ni–YSZ anodes at 500° C in solid oxide fuel cells by electrochemical impedance analysis, J. Korean Ceram. Soc. 58 (2021) 606–613.

[40] J.-h Myung, D. Neagu, D.N. Miller, J.T. Irvine, Switching on electrocatalytic activity in solid oxide cells, Nature 537 (2016) 528.

[41] N. Hou, T. Yao, P. Li, X. Yao, T. Gan, L. Fan, J. Wang, X. Zhi, Y. Zhao, Y. Li, A-site ordered double perovskite with in situ exsolved core–shell nanoparticles as anode for solid oxide fuel cells, ACS Appl. Mater. Interfaces 11 (2019) 6995–7005.

[42] Z. Du, H. Zhao, S. Li, Y. Zhang, X. Chang, Q. Xia, N. Chen, L. Gu, K. Świerczek, Y. Li, Exceptionally high performance anode material based on lattice structure decorated double perovskite Sr2FeMo2/3Mg1/3O6− δ for solid oxide fuel cells, Adv. Energy Mater. (8) (2018) 1800062.

[43] T. Zhu, H.E. Troiani, L.V. Mogni, M. Han, S.A. Barnett, Ni-substituted Sr(Ti,Fe)O 3 SOFC anodes: achieving high performance via metal alloy nanoparticle exsolution, Joule 2 (2018) 478–496.

[44] C. Yang, Z. Yang, C. Jin, G. Xiao, F. Chen, M. Han, Sulfur-tolerant redox-reversible anode material for direct hydrocarbon solid oxide fuel cells, Adv. Mater. 24 (2012) 1439–1443.

[45] T. Zhu, D.E. Fowler, K.R. Poeppelmeier, M. Han, S.A. Barnett, Hydrogen oxidation mechanisms on perovskite solid oxide fuel cell anodes, J. Electrochem. Soc. 163 (2016) F952.

[46] L. Bian, C. Liu, S. Li, J. Peng, X. Li, L. Guan, Y. Liu, J.H. Peng, S. An, X. Song, Highly stable La0. 5Sr0. 5Fe0. 9Mo0. 1O3-δ electrode for reversible symmetric solid oxide cells, Int. J. Hydrog. Energy (2020).

[47] Y. Wang, T. Liu, M. Li, C. Xia, B. Zhou, F. Chen, Exsolved Fe–Ni nano-particles from Sr 2 Fe 1.3 Ni 0.2 Mo 0.5 O 6 perovskite oxide as a cathode for solid oxide steam electrolysis cells, J. Mater. Chem. A 4 (2016) 14163–14169.

[48] Z. Teng, Z. Xiao, G. Yang, L. Guo, X. Yang, R. Ran, W. Wang, W. Zhou, Z. Shao, Efficient water splitting through solid oxide electrolysis cells with a new hydrogen electrode derived from A-site cation-deficient La0. 4Sr0. 55Co0. 2Fe0. 6Nb0. 2O3-δ perovskite, Mater. Today Energy (2020), 100458.

[49] C. Jin, C. Yang, F. Zhao, D. Cui, F. Chen, La0. 75Sr0. 25Cr0. 5Mn0. 5O3 as hydrogen electrode for solid oxide electrolysis cells, Int. J. Hydrog. Energy 36 (2011) 3340–3346.

[50] Q. Liu, C. Yang, X. Dong, F. Chen, Perovskite Sr2Fe1. 5Mo0. 5O6− δ as electrode materials for symmetrical solid oxide electrolysis cells, Int. J. Hydrog. Energy 35 (2010) 10039–10044.

[51] C. Yang, Z. Yang, C. Jin, M. Liu, F. Chen, High performance solid oxide electrolysis cells using Pr0. 8Sr1. 2 (Co, Fe) 0.8 Nb0. 2O4+ δ–Co–Fe alloy hydrogen electrodes, Int. J. Hydrog. Energy 38 (2013) 11202–11208.

[52] C. Yang, C. Jin, A. Coffin, F. Chen, Characterization of infiltrated (La0. 75Sr0. 25) 0.95 MnO3 as oxygen electrode for solid oxide electrolysis cells, Int. J. Hydrog. Energy 35 (2010) 5187–5193.

[53] T. Liu, Y. Wang, Y. Zhang, S. Fang, L. Lei, C. Ren, F. Chen, Steam electrolysis in a solid oxide electrolysis cell fabricated by the phase-inversion tape casting method, Electrochem. Commun. 61 (2015) 106–109.